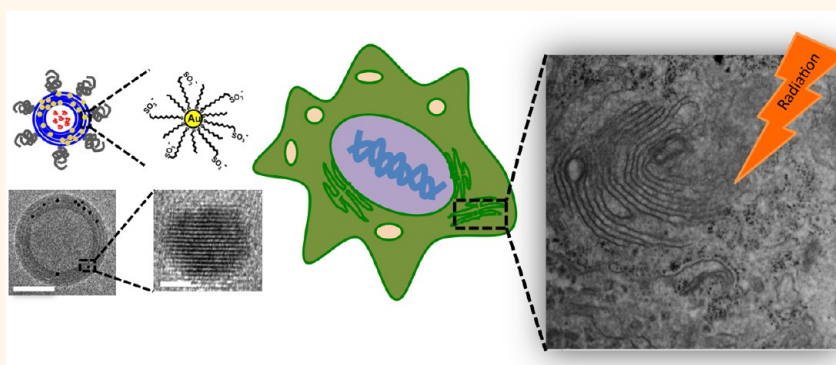# Enhancing Radiotherapy by Lipid Nanocapsule-Mediated Delivery of Amphiphilic Gold Nanoparticles to Intracellular Membranes

Yu-Sang Yang,[†] Randy P. Carney,[§] Francesco Stellacci,[§] and Darrell J. Irvine[†,‡,∥,⊥,#,⊗,*]

[†]Department of Materials Science and Engineering, [‡]Department of Biological Engineering, [⊥]Institute for Soldier Nanotechnologies, and [#]Koch Institute for Integrative Cancer Research, Massachusetts Institute of Technology, Cambridge, Massachusetts 02139, United States, [§]Institute of Materials Science and Engineering, École Polytechnique Fédérale de Lausanne, 1015 Lausanne, Switzerland, [∥]Ragon Institute of MGH, MIT, and Harvard, Charlestown, Massachusetts 02129, United States, and [⊗]Howard Hughes Medical Institute, Chevy Chase, Maryland 20815, United States

ABSTRACT

Amphiphilic gold nanoparticles (amph-NPs), composed of gold cores surrounded by an amphiphilic mixed organic ligand shell, are capable of embedding within and traversing lipid membranes. Here we describe a strategy using crosslink-stabilized lipid nanocapsules (NCs) as carriers to transport such membrane-penetrating particles into tumor cells and promote their transfer to intracellular membranes for enhanced radiotherapy of cancer. We synthesized and characterized interbilayer-crosslinked multilamellar lipid vesicles (ICMVs) carrying amph-NPs embedded in the capsule walls, forming Au-NCs. Confocal and electron microscopies revealed that the intracellular distribution of amph-NPs within melanoma and breast tumor cells following uptake of free particles *vs* Au-NCs was quite distinct and that amph-NPs initially delivered into endosomes by Au-NCs transferred over a period of hours to intracellular membranes through tumor cells, with greater intracellular spread in melanoma cells than breast carcinoma cells. Clonogenic assays revealed that Au-NCs enhanced radiotherapeutic killing of melanoma cells. Thus, multilamellar lipid capsules may serve as an effective carrier to deliver amphiphilic gold nanoparticles to tumors, where the membrane-penetrating properties of these materials can significantly enhance the efficacy of frontline radiotherapy treatments.

Radiation therapy remains a frontline treatment in cancer therapy and is used to treat breast,[1] cervical,[2] skin,[3] lung,[4] and brain[5] cancers, to name just a few. Radiation can be applied to the entire body or to specific tissue sites and causes radiolytic hydrolysis inside living cells—an ionization cascade that produces high transient concentrations of hydroxyl radicals, peroxides, and other highly reactive species that damage proteins and genetic material, weakening or killing affected cells.[6] Radiation also interacts with and denatures biomacromolecules directly; however, this effect is less significant. The essential concept of radiotherapy is to cause damage to cancer cells at a higher rate than to healthy tissues—accepting that some damage to healthy tissues will occur. Thus, radiotherapy inherently involves a balance between

maximizing damage to target tissues and minimizing damage to healthy tissues. Localized treatment can be used to focus radiation therapy on tumor tissues, but toxicity to nearby healthy tissue remains the key factor limiting the dose of radiation that can be administered. Tomotherapy[7] and image-guided radiation therapy (IGRT)[8] better concentrate the dose within the shape of the lesion and produce steep dose gradients. Despite these advances, radiotherapy often fails to fully eradicate tumors due to dose limitations and some tumors' insensitivity to radiation.

One strategy to increase the therapeutic index of radiation therapy is through the use of radiosensitizers. For example, Santos Mello et al. reported that intratumoral iodine contrast agent injection followed by 100 kVp X-rays completely suppressed growth in 80% of mouse tumors in vivo. However, iodine radiosenitization is limited by its rapid clearance.[9] Current investigations seek to improve cancer therapy via the use of synthetic nanomaterials for prolonged circulation half-life and better tumor targeting efficiency. Synthetic metallic nanomaterials have been explored as agents to amplify cancer therapeutic modalities such as hyperthermia,[10] laser ablation,[11] and radiation therapy,[12] due to their ability to interact strongly with externally-applied fields. Metallic nanomaterials have particularly found application as adjuvants to radiotherapy due to their strong interaction with ionizing radiation. Germanium nanoparticles,[13] iron oxide nanoparticles,[14] and platinum complexes[15] have been demonstrated as adjuvants for enhanced cellular radiosensitivity.

Gold nanoparticles have properties well suited to radiosensitization: their high atomic number (Z), biocompatibility, precisely controllable size, and tunable surface functionalization.[16−23] High-Z elements have higher X-ray interaction cross-sections than light organic elements (H, O, N, C), increasing energy deposition and radiolytic hydrolysis in the immediate vicinity of these materials. Increasing homogeneity of the intracellular distribution of gold nanoparticles has been previously hypothesized to correlate with increasing radiosensitization.[24] Gold nanoparticles used in biomedical applications are typically solubilized in aqueous solution via sheathing within an organic ligand layer. In the present work, we focused on amphiphilic gold nanoparticles (amph-NPs) where the organic ligand shell is composed of a 1:1 mixture of alkanethiol ligands terminated by hydrophilic (11-mercaptoundecanesulfonate, MUS) and hydrophobic (octanethiol, OT) functional groups (Scheme 1).[25,26] We previously showed that such amph-NPs can enter live cells through both energy-dependent and-independent pathways without inducing membrane poration or toxicity.[26−28] Recently, we have begun to understand the mechanisms underlying cellular entry by these nanomaterials th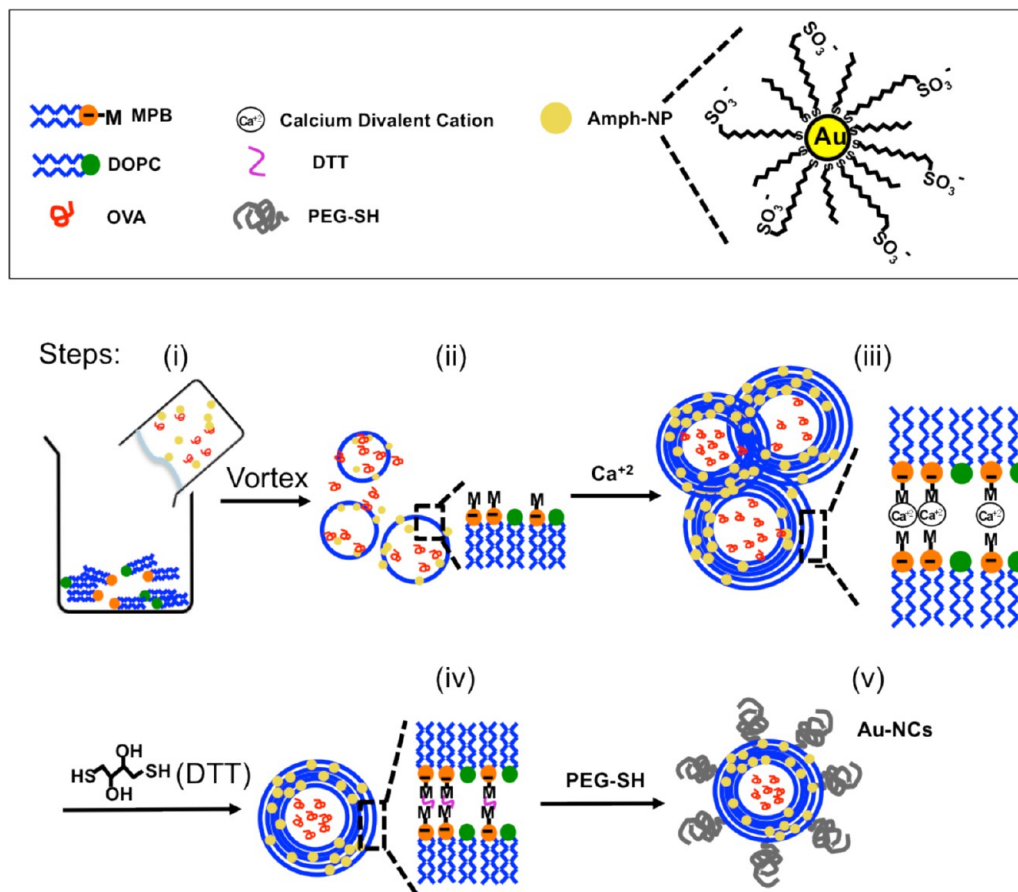rough combined computational modeling and experiments demonstrating that the particles embed within lipid membranes through splaying of ligands in the organic shell to allow hydrophobic matching with the bilayer.[29]

Motivated by these findings, we hypothesized that amph-NPs could be effective radiosensitizers, as they might not only disperse throughout cells to spread radiation damage but also concentrate X-ray energy in intracellular membranes to enhance damage to target tumor cells. However, in vivo applications would require selective targeting of these membrane-penetrating particles to disease sites. Nanoparticles in the 30−300 nm size range are known to accumulate in tumors via the enhanced permeation and retention effect.[30,31] Thus, to ferry these membrane-penetrating particles to tumors and promote tumor cell uptake, here we describe packaging of amph-NPs within the lipid walls of interbilayer-crosslinked multilamellar lipid vesicles (ICMVs). ICMVs[32] are multilayer lipid nanocapsules recently developed in our laboratory that possess significantly more bilayer area than an equivalent radius monolayer lipid vesicle (e.g., liposomes), giving ICMVs a high amph-NP loading capacity and increased stability relative to traditional multilamellar vesicles. In previous work, we demonstrated that ICMVs show greatly enhanced stability relative to liposomes or multilamellar vesicles in serum, which correlated with enhanced lymph node delivery of antigens in the setting of vaccination.[32] We hypothesized that ICMVs could transport amph-NPs to tumor cells, followed by endocytic uptake of the lipid capsules; disruption of ICMVs within endolysosomes would lead to release of amph-NPs and transfer of the membrane-penetrating particles to intracellular membranes of the target cells.

Here, we focused as a first step on characterizing at the single-cell level in vitro how amph-NPs are taken up by tumor cells when administered as free particles or packaged into ICMVs, and tested the resultant killing efficiency under radiotherapy for two types of murine cancer cells—melanoma (B16F10 cells) and breast carcinoma (4T1 cells). The intracellular distribution of amph-NPs delivered as free soluble amph-NPs or via ICMV was observed via confocal microscopy and thin-section TEM (transmission electron microscopy) to be delivery-mechanism and cell-type dependent, with Au-NCs showing the greatest enhancement of radiotherapy in melanoma cells where delivery of amph-NPs throughout the cytoplasm and intracellular membranes was observed.

RESULTS AND DISCUSSION

ICMV nanocapsules are formed by fusion of anionic, maleimide-functionalized lipid vesicles with divalent cations, followed by addition of a membrane-permeable crosslinker (dithiothreitol (DTT)) that diffuses between the membranes and covalently crosslinks maleimide lipids of adjacent bilayers forming the capsule wall.[32]

Scheme 1. Au-NC Synthesis[a]

[a] (i) Dried lipid films composed of 50% DOPC 50% MPB-PE rehydrated with buffer containing amph-NPs and OVA protein, forming (ii) gold-embedded/protein-encapsulated liposomes. (iii) Anionic liposomes fused by addition of calcium. (iv) Stacked lipid bilayers were crosslinked by addition of DTT and (v) outer surfaces PEGylated.

To load gold nanoparticles in the capsule walls, we added amph-NPs to the aqueous buffer during rehydration of dried lipids, with the goal of forming precursor liposomes with amph-NPs embedded in the vesicle bilayers (Scheme 1). We also included fluorescent ovalbumin (OVA) protein in the aqueous phase during lipid hydration as a model co-delivered drug cargo and tracer to label the aqueous core of the ICMVs. Fusion of the gold-loaded precursor vesicles and crosslinking the bilayers with DTT led to gold-loaded ICMV nanocapsules (Au-NCs). The remaining maleimide groups at the surfaces of the particles were quenched by capping with PEG-thiol to enhance the colloidal stability of the nanocapsules.

To examine gold particle entrapment efficiency, we loaded 2.2 ± 0.5 nm diameter core amph-NPs (Supporting Information, Figure S1) into ICMVs. The MUS and OT ligands protecting the gold core span approximately 1.6 nm, resulting in a total hydrodynamic diameter of 5.4 nm that is similar to the thickness of a lipid bilayer (4–5 nm).[33,34] Post-PEG capping, the Au-NCs were spun down and the supernatant was

collected; absorbance measurements on these supernatants showed no detectable unentrapped gold remaining in the aqueous phase. Quantitative analysis of the loading efficiency of 2.2 nm core amph-NPs into ICMV capsules was performed via UV−vis and infrared spectrometry. As shown in Table 1, gold loading increased with increased concentrations of added amph-NPs, while the tracer OVA protein encapsulation decreased with increased Au loading.

Transmission electron microscopy (TEM) images of Au-NCs dried on carbon/formvar-coated copper grids showed that almost no free gold particles were present in Au-NC samples; the vast majority of the nanoparticles were associated with lipid capsules (Figure 1a,b). Consistent with our prior studies suggesting that amph-NPs have a high affinity for membranes,[28] cryo-electron microscopy analysis of Au-NCs in vitrified solution (Figure 1c) showed that amph-NPs localized to the stacked lipid layers of the capsule walls and free particles were not detected in the aqueous cores of the capsules. Larger multilamellar ICMV capsules appeared to contain higher amounts of amph-NPs relative to

TABLE 1. Quantitative Analysis of Gold and Protein Loading in ICMVs as a Function of Cargo Concentration

amph-NP/OVA cargos added to synthesis	lipid capsule size[a] (nm)	OVA encapsulated (μg/mg lipid)	amph-NPs encapsulated (mg/mg lipid)
0.28 mg/mL amph-NPs, 300 μg/mL OVA	242 ± 151	24.26	0.31 ± 0.024
0.7 mg/mL amph-NPs, 300 μg/mL OVA	236 ± 32	20.45	0.35 ± 0.012
1.13 mg/mL amph-NPs, 300 μg/mL OVA	254 ± 39	13.41	0.59 ± 0.021
no amph-NPs, 300 μg/mL OVA	207 ± 67	67.27	N/A
no amph-NPs, no OVA	160 ± 23	N/A	N/A

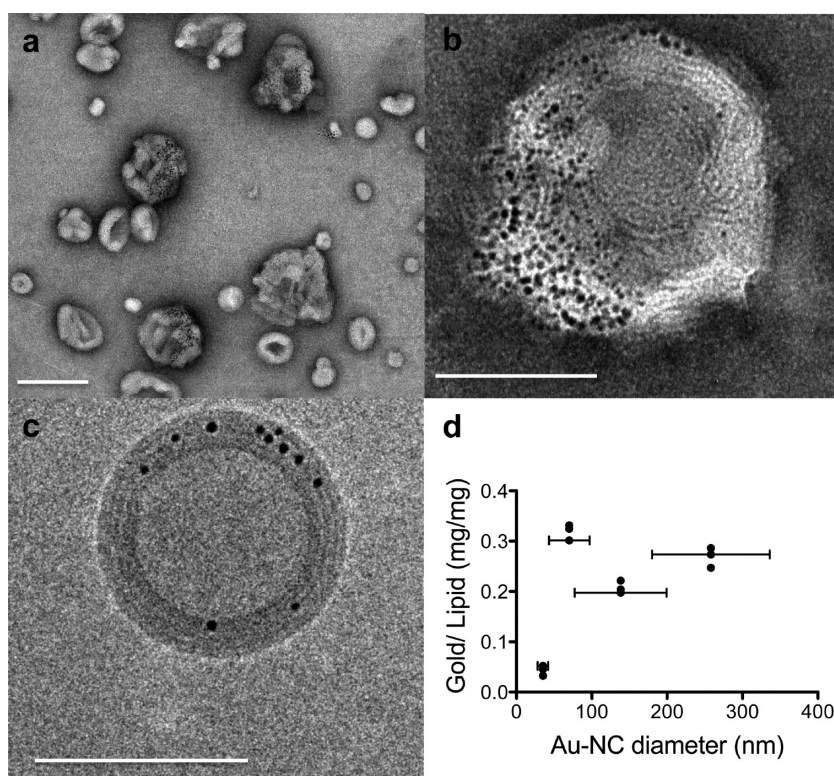[a] Measured by dynamic light scattering.

Figure 1. TEM and Cryo-TEM micrographs of Au-NCs with encapsulated OVA. (a, b) Au-NCs were dried on grids followed by negative staining with phosphotunstic acid and TEM imaging. Scale bars 200 nm (a), 100 nm (b). (c) Cryo-TEM of Au-NCs in water (scale bar 100 nm). (d) Gold to lipid mass ratios as a function of NC diameter measured for a preparation of nanocapsules divided into four different size fractions. Error bars show the standard deviation of each size fraction.

smaller nanocapsules in the preparation. To characterize the degree of heterogeneity of gold particle loading in different sized nanocapsules, we used size fractionation to isolate four different mean sizes of Au-NCs from a single preparation of Au-NCs and measured the gold/lipid mass ratio in each fraction. As shown in Figure 1d, Au-NCs with diameters less than 50 nm showed a ~3-fold decrease in gold loading compared to larger Au-NCs, but larger particles all contained 0.2-0.3 mg of gold/mg lipid.

To examine the interaction of amph-NPs and Au-NCs with tumor cells, we employed two cell lines representative of cancer types where radiation therapy is an important treatment modality: B16F10 melanoma cells and 4T1 breast cancer cells. First, viability of both cell types 24 h post-treatment with free amph-NPs, empty nanocapsules, or Au-NCs was evaluated by flow cytometry. The cells were transduced with GFP for the ease

of determination of the live cell population; dying or dead cells were stained with DAPI. As shown in Figure S2 (Supporting Information), all treatments at doses as high as 250 nM amph-NPs (0.11 mM lipids and 250 nM amph-NPs for Au-NCs) yielded >80% cell viability. Thus, the amph-NPs and lipid carriers show little toxicity per se to these tumor lines, consistent with prior toxicity measurements made on a variety of other cell types with these particles.[26,27,35] We next characterized the internalization and intracellular distribution of fluorescently-labeled amph-NPs or amph-NP-loaded lipid capsules. For B16F10 cells, gold uptake in the form of free amph-NPs or Au-NCs added to the medium was first quantified by flow cytometry. Incubation of either free amph-NPs or Au-NCs with B16F10 cells led to high levels of Au uptake within all cells in the population (Figure 2a). Confocal microscopy showed a homogeneous distribution of free amph-NPs within the
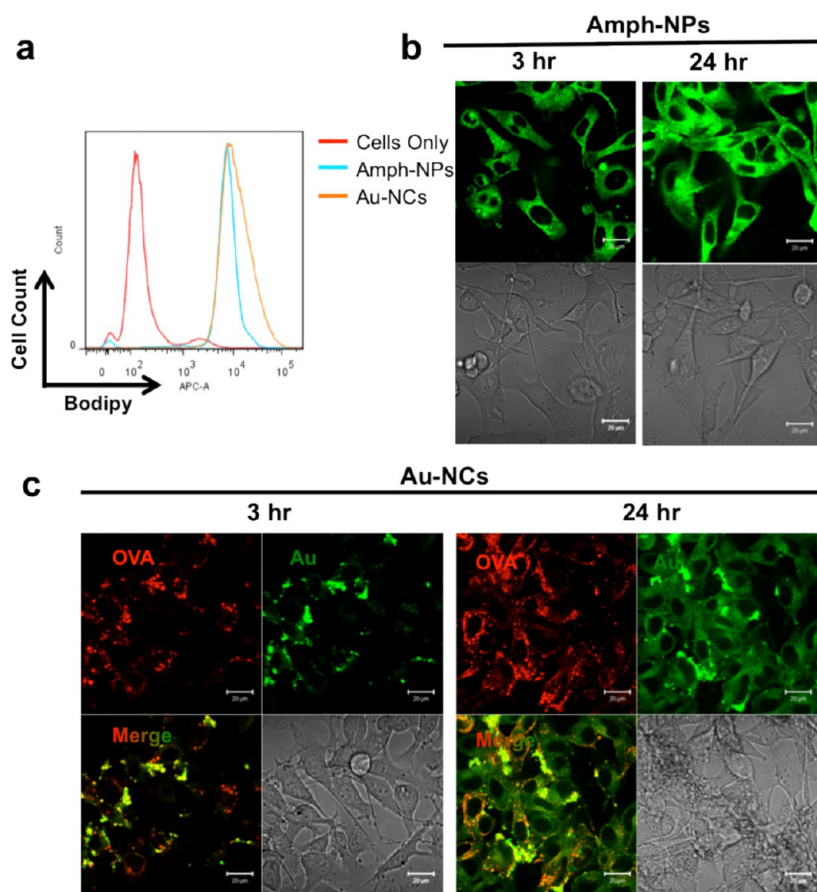
Figure 2. Uptake of amph-NPs and Au-NCs by B16F10 melanoma cells. (a) Flow cytometry analysis of bodipy-labeled gold NP uptake after 24 h incubation with 250 nM Au particles (free amph-NPs or equivalent amounts of amph-NPs loaded in ICMV capsules). (b, c) B16F10 cells were incubated with 250 nM Au (green) as free amph-NPs (b) or loaded in ICMV capsules (c) and then imaged after 3 or 24 h by confocal microscopy. ICMVs were co-labeled by encapsulated fluorescent ovalbumin protein (red, c). (Scale bars 20 μm).

cytoplasm of B16F10 cells (but excluded from cell nuclei) at both 3 and 24 h time points (Figure 2b). By contrast, amph-NPs delivered *via* lipid capsules were initially confined in endosomes with obvious punctate spots after 3 h of incubation with cells. In preliminary studies, we confirmed that fluorophore-labeled OVA can reliably mark the location of the lipid capsules intracellularly—encapsulated OVA remained colocalized with fluorescent lipid NBD-PC incorporated in ICMVs. Amphiphilic gold nanoparticles amph-NPs) were always co-localized with OVA fluorescence, suggesting that they remained associated with the lipid nanocapsules at this early time point (Figure 2c). However, after 24 h, amph-NPs were distributing through the cytoplasm of cells, while OVA signals remained punctate (presumably confined to endosomes, Figure 2c). These data suggest that amph-NPs can pass out of the ICMV nanocapsules into the cytosol or internal membranes of cells without overt disruption of endosomes, as endosomal rupture would have led OVA to also disperse into the cytosol.

Similar to the results with B16F10, both amph-NPs and Au-NCs were taken up in high levels by 4T1 breast tumor cells when analyzed by flow cytometry (Figure 3a). In confocal imaging, 4T1 cells treated with

free amph-NPs showed punctate signals in addition to a dim cytoplasmic signal at both 3 and 24 h of incubation, suggesting partitioning between endosomes and the cytoplasm (Figure 3b). Strikingly, when 4T1 cells were incubated with Au-NCs, the protein and amph-NPs signals remained co-localized in punctate structures in the cells through 24 h, suggesting that in these tumor cells, the majority of amph-NPs remained trapped in endosomes, at least through this time point.

To assess the subcellular distribution of amph-NPs delivered into each of the tumor cell lines, we also carried out TEM imaging on thin sections of treated cells. Free amph-NPs incubated with B16F10 cells for 24 h were found both dispersed in the cytosol (block arrows, Figure 4a) and associated with endosomal structures (line arrows, Figure 4a). Notably, amph-NPs trapped in endosomes of these cells appeared to be associated with/surrounded by electron-dense material, suggesting association with lipid or proteins within the endosomes, as highlighted by the arrows in Figure 4b. By contrast, B16F10 cells incubated for 3 h with Au-NCs showed apparent unraveling ICMV capsules within endosomes, and amph-NPs were still confined in these endosomes at this time point, in
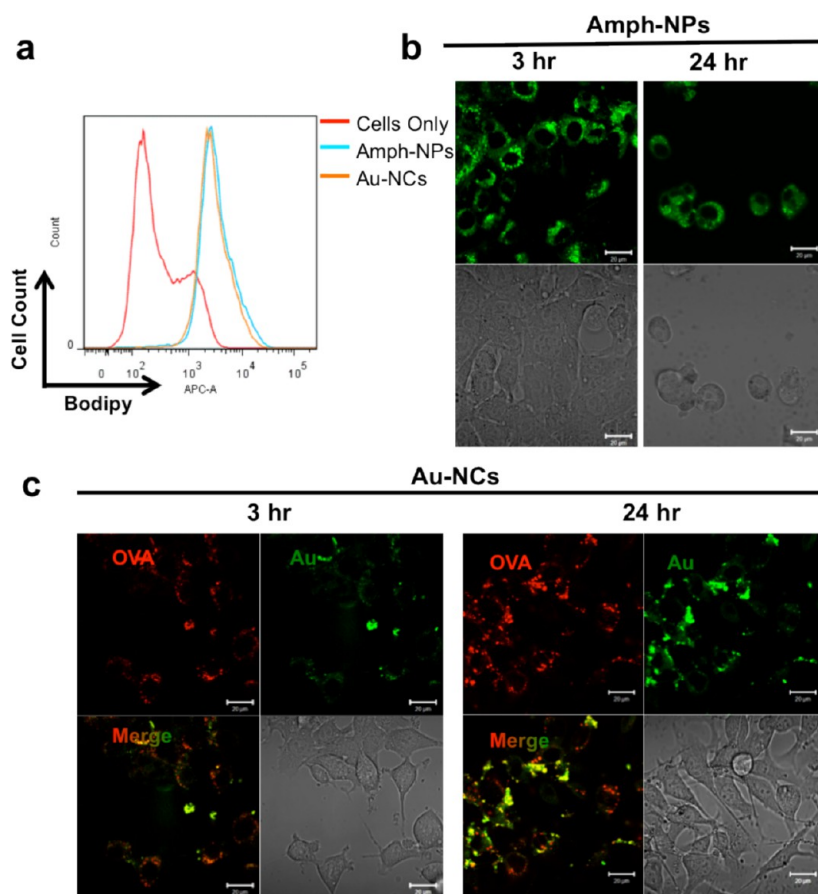
Figure 3. Uptake of amph-NPs and Au-NCs by 4T1 breast carcinoma cells. (a) Flow cytometry analysis of bodipy-labeled gold NP uptake after 24 h incubation with 250 nM Au particles (free amph-NPs or equivalent amounts of amph-NPs loaded in ICMV capsules). (b, c) 4T1 cells were incubated with 250 nM Au (green) as free amph-NPs (b) or loaded in ICMV capsules (c) and then imaged after 3 or 24 h by confocal microscopy. ICMVs were co-labeled by encapsulated fluorescent ovalbumin protein (red, c). (Scale bars 20 μm).

agreement with the confocal data (Figure 4c). However, after 24 h, the vast majority of amph-NPs were found delocalized away from ICMV capsule fragments; amph-NPs were found dispersed into the cytosol and associated with distant intracellular membranes (Figure 4d). Whether taken up as free particles or Au-NCs, amph-NPs were not observed to associate with mitochondrial or nuclear membranes.

In 4T1 cells, TEM images revealed quite distinct distributions of the amph-NPs. Free amph-NPs were detected associated with both the plasma membranes and cytosolic cellular membranes of these cells, as shown in Figure 5a,b. However, the majority of amph-NPs were localized within in multivesicular endosomes as shown in Figure 5c. In agreement with the confocal imaging results, 4T1 cells that internalized Au-NCs showed little detectable amph-NP dispersion outside of large endosomes where the ICMV lipid capsules were trapped even after 24 h (Figure 5d). Thus, the fate of the membrane-penetrating amph-NPs at the subcellular level was dependent both on the mode of cellular uptake (free or lipid capsule delivered) and the tumor cell type.

We hypothesized that the distinct behavior of amph-NPs in the two tumor cell types may reflect a more substantial glycocalyx present on the plasma membrane and interior membranes of endosomes of epithelium-derived 4T1 cancer cells[36] compared to the melanocyte-derived B16 tumor cells. To confirm that this is a key distinction between the cell surface chemistry of B16F10 and 4T1 cells, we labeled the cells with fluorophore-conjugated wheat germ agglutinin (WGA), a lectin that binds sugars of the glycocalyx. As shown in Figure 6a,b, WGA staining confirmed that 4T1 cells have a much more substantial glycocalyx lining the plasma membrane, which may form a barrier to amph-NP penetration through the cell surface or endosomal membranes. To determine whether this trend holds in other cell types, we also assessed the intracellular distribution of Au-NCs in two other tumor cell lines, MC38 (an epithelial colon adenocarcinoma) and LLC (an epithelial Lewis lung adenocarcinoma). As shown in Supplemental Figures 3 and 4 (Supporting Information), the glycocalyx density of these two other tumor cells was intermediate between 4T1 and B16F10, and the intracellular distribution of gold
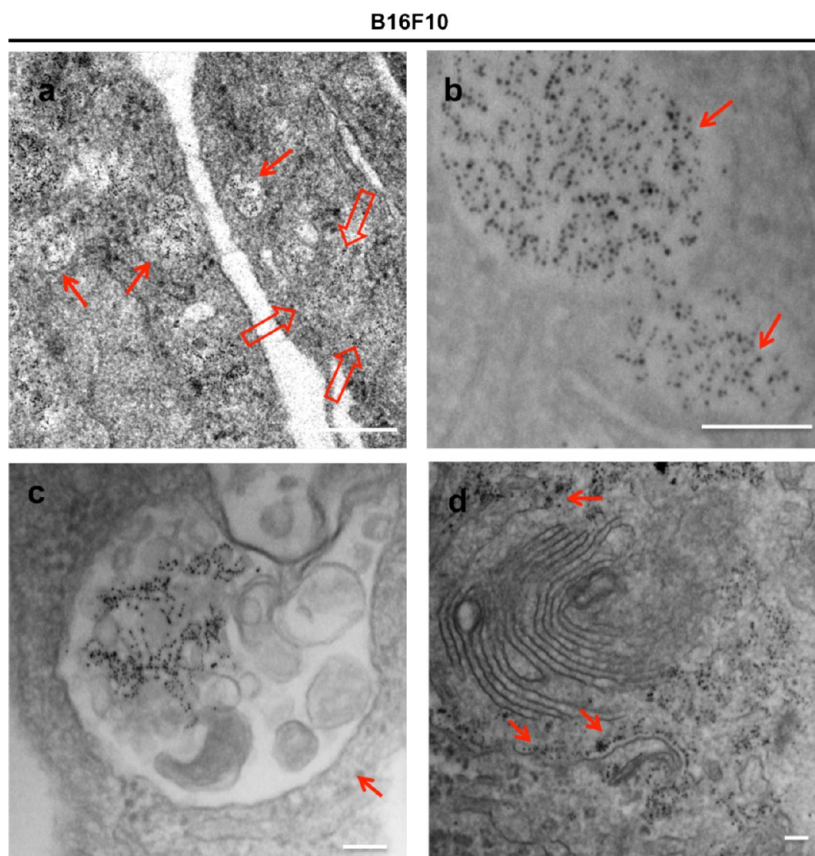
B16F10

Figure 4. Thin-sectioned TEM images of B16F10 melanoma cells incubated with free amph-NPs or Au-NCs for 24 h: (a,b) amph-NPs (scale bars 250 nm(a), 100 nm (b)); (c, d) Au-NCs (scale bars 100 nm). Line arrows in (a) highlight amph-NPs in endosomes; Block arrows in (a) highlight amph-NPs dispersed in the cytosol.

particles was also intermediate between the complete cytosolic dissemination observed with B16F10 melanoma cells and the complete endosomal entrapment seen with 4T1 cells; LLC tumor cells that had higher WGA staining showed more endosomal entrapment of amph-NPs. We quantified the degree of colocalization between fluorophore-conjugated OVA protein delivered into endosomes by ICMVs *vs* the co-delivered amph-NPs by measuring a colocalization index (Pearson's correlation coefficient) for intensity of OVA signal *vs* amph-NP signal at a given pixel in a set of confocal microscopy images for each cell type. As shown in Supplemental Figure 5a,b (Supporting Information), there was a clear correlation between the strength of glycocalyx staining and the degree of endosomal entrapment (OVA colocalization) for amph-NPs delivered by the lipid nanocapsules. Thus, the ability of amph-NPs to escape ICMV nanocapsules and disseminate to the cytosol appears to be regulated by the glycocalyx density on tumor cells. However, the precise role of the glycocalyx will need to be further studied in future work, as there may be additional governing parameters involved in amph-NP uptake and the glycocalyx is only one factor among many that is distinct between the four cell lines tested here.

Irradiated gold nanoparticles enhance the therapeutic anti-tumor efficacy of X-ray and gamma ray irradiation *via* generation of auger electrons and photoelectrons that amplify the X-ray interaction with the tissue. Gold nanoparticles increase the energy deposition achieved by irradiation and promote pronounced radiation damage in their immediate vicinity due to the short range travelling distance (2−4 nm) of emitted electrons, which cause both radiolysis of water and direct damage to biomacromolecules. To determine the efficacy of radiosensitization *via* free amph-NPs or Au-NCs, B16F10 and 4T1 tumor cells were treated with gold nanoparticles in either form (or left untreated as controls), irradiated for a total dose of 4 Gy using a ^{137}Cs gamma irradiator, and a clonogenic assay[37] was used to assess the resulting impact on tumor cell growth as a quantitative measure of single tumor cells' abilities to grow into a colony post-treatment. Tumor cell colony growth after irradiation was significantly reduced relative to untreated cells (Figure 7a), though B16F10 cells were substantially more resistant to irradiation than the 4T1 cells (Figure 7b). 4T1 cells were quite sensitive to radiation treatment, and amph-NPs did not enhance irradiation-mediated killing of these cells; treatment with Au-NCs gave a trend toward decreased 4T1 viability that did
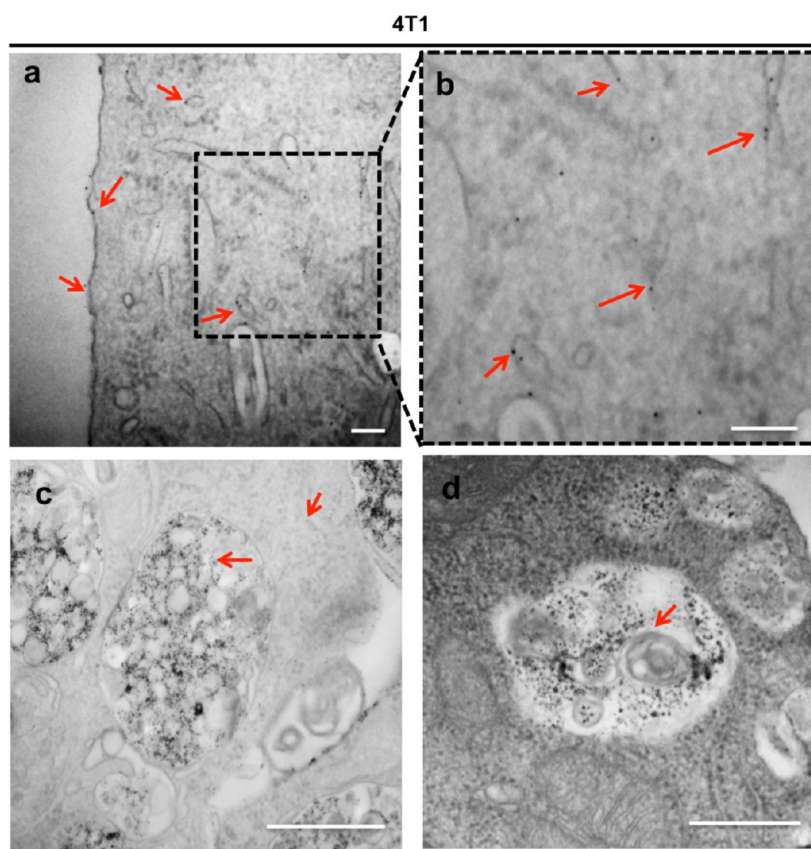
4T1

Figure 5. Thin-sectioned TEM images of 4T1 breast cancer cells incubated with free amph-NPs (a−c) or Au-NCs (d) for 24 h (scale bars (a, b) 100 nm, (c, d) 500 nm). Arrows highlight amph-NPs dispersed among endosomal and intracellular membranes.

not reach statistical significance. In contrast, both amph-NPs and Au-NCs enhanced irradiation-mediated killing of B16F10 cells, with Au-NCs leading to a >3-fold increase in tumor cell killing relative to irradiation alone. The greater efficacy of Au-NCs over free amph-NPs in this *in vitro* assay may reflect the slightly greater total gold delivery into the cells mediated by the nano-capsules (Figure 2a) or subtle alterations in the intra-cellular disposition of the ICMV-delivered gold.

CONCLUSIONS

In summary, we have demonstrated here a strategy to package amphiphilic, membrane-embedding gold nanoparticles into multilamellar lipid capsules for delivery and enhanced radiosensitization in tumor cells. The subcellular distribution of amph-NPs depended on the cell type, with membrane-penetrating particles accumulating both in endosomes and cytosolic structures in B16F10 melanoma cells but exhibiting a more limited dispersion to intracellular membranes in epithelium-derived 4T1 breast carcinoma cells. De-creased glycocalyx thickness is observed in this work to correlate with increased endosomal escape of nano-capsule-delivered amph-NPs. Amph-NPs delivered into melanoma cells by lipid nanocapsules were initi-ally confined to endosomes, but over time, the amph-NPs dispersed throughout the cells in a manner similar to the cellular penetration of free amph-NPs *in vitro*. Reflecting the differences in intracellular distribution, Au-NCs were more effective in enhancing melanoma tumor cell killing than 4T1 cell killing, with a 3-fold increase in tumor cell death relative to irradia-tion alone. As the lipid capsules described here are PEGylated and may potentially be further functionalized with ligands to direct tumor cell binding, Au-NCs may provide a means to direct cell-penetrating gold nano-particles to tumor cells *in vivo* for enhancement of frontline radiation therapy in a variety of cancers.

MATERIALS AND METHODS

Synthesis of Amph-NPs. As described in our previous work,[26] 0.9 mmol of $HAuCl_4$ (Sigma-Aldrich) was dissolved in 200 mL of ethanol, 0.9 mmol of the desired thiol ligand mixture was added while the reaction solution was stirred, and then a saturated ethanol solution of sodium borohydride ($NaBH_4$) was added dropwise for 2 h. The solution was stirred for 3 h, and the reaction vessel was then placed in a refrigerator overnight; precipitated particles were collected *via* vacuum filtration with quantitative filter paper. The residue was washed with ethanol, methanol, and acetone and dried under vacuum. To completely remove unbound ligands, particles were dialyzed using 5 in.
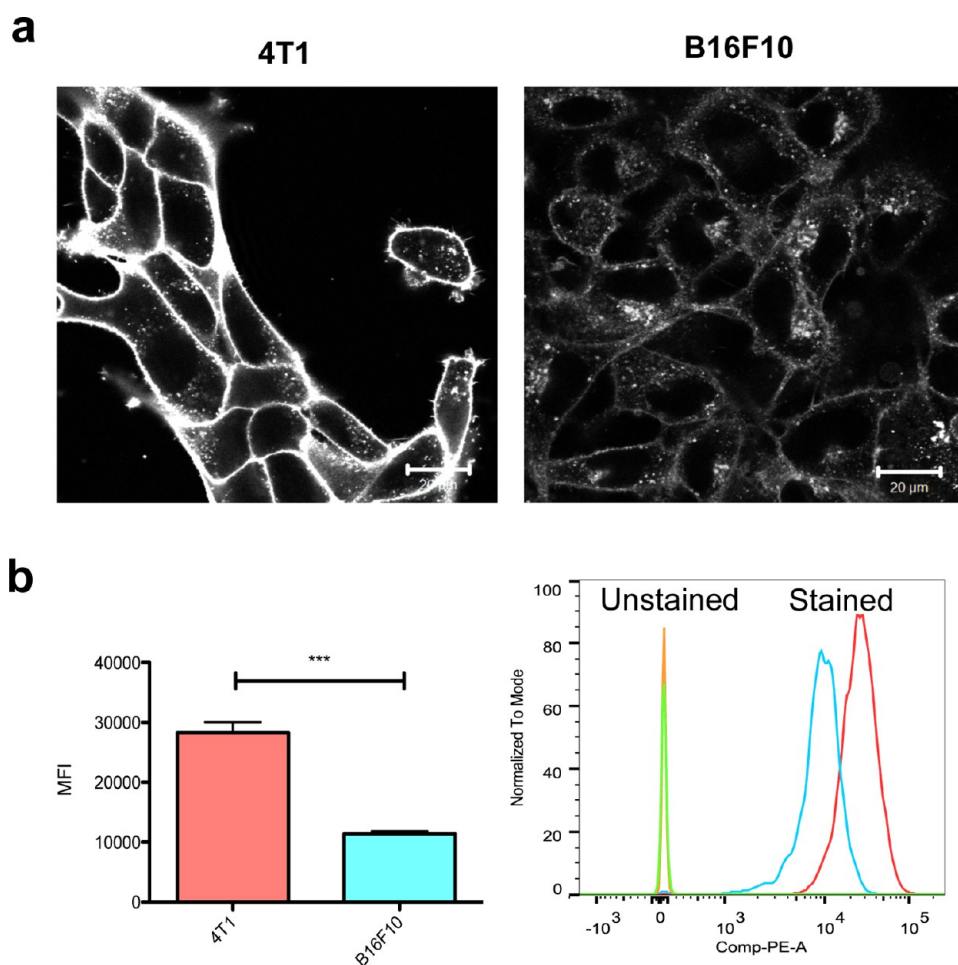
Figure 6. (a) Confocal images of the glycocalyx of B16F10 and 4T1 cells labeled with AF555-Wheat Germ Agglutinin (WGA). (b) Flow cytometry quantification of WGA-labeled tumor cells. ***, $P = 0.0007$ by unpaired t test.

segments of cellulose ester dialysis membrane (Pierce, MWCO 3500) that were placed in 1 L beakers of Milli-Q water and stirred slowly. The beakers were recharged with fresh DI water ca. every 8 h over the course of 72 h. The NP solutions were collected from the dialysis tubes, and the solvent was removed under vacuum at <45°C.

Fluorescence Dye Labeling of Amph-NPs. To track gold nanoparticles by fluorescence microscopy, amph-NPs were labeled with a thiolated BODIPY dye as previously described.[26] Briefly, 5 μL of BODIPY-SH (2.45 mg/mL in 2:1 water/dimethylformamide mixture) was added to 10 mg of gold nanoparticles in 1 mL of water. The solution was covered with foil to protect it from light and agitated at speed of 750 rpm on a shaker for 3−4 days at 25°C. Unconjugated BODIPY-SH was completely removed by topping up the eppendorf with acetone and centrifuging at 14kg for 2 min (repeated four times). Excess acetone was evaporated in a vacuum oven overnight. The dried nanoparticles were dissolved in water, and nanoparticle concentrations were determined by reading the absorbance at 520 nm.

Synthesis and Characterization of Au-NCs. Lipids in chloroform (1.26 μmol total lipid, 1:1 molar ratio of 1,2-**dio**leoyl-*sn*-glycero-3-**p**hospho**c**holine (DOPC) and 1,2-dioleoyl-*sn*-glycero-3-phosphoethanolamine-*N*-[4-(*p*-maleimidophenyl)butyramide] (MPB PE), all lipids from Avanti Polar Lipids, Alabaster, AL) were dispensed to glass vials, and the organic solvents were evaporated under vacuum overnight to prepare dried thin lipid films. Lipid films were rehydrated in 10 mM bis-tris propane buffer (pH 7.0) containing amph-NPs and ovalbumin (Life Technologies) at the indicated concentrations for 1 h with rigorous vortexing every 10 min and then sonicated in alternating power cycles of 6 and 3 W at 30 s intervals for 5 min on ice (Misonix Microson XL probe tip sonicator, Farmingdale, NY). The liposomes formed in this first step were induced to undergo fusion by addition of CaCl$_2$ at a final concentration of 10 mM. The resulting multilamellar vesicles were incubated with 1.5 mM DTT (maleimide/DTT molar ratio of 2:1) for 1 h at 37 °C to conjugate opposing bilayers of maleimide-functionalized lipids and form crosslinked nanocapsules; the resulting vesicles were recovered by centrifugation at 14000g for 4 min and washed twice with deionized water. Finally, the Au-NCs (0.3 mg/mL lipids) were incubated with 2 kDa PEG-SH (Laysan Bio, Arab, AL) in a 3-fold molar excess of PEG-SH to maleimide groups for 1 h at 37 °C to PEGylate the particle surfaces. As-synthesized Au-NCs were diluted twice and passed through a sterile filter twice (200 nm membrane Acrodisc Syringe Filter with HT Tuffryn Membrane, Pall Filters) to remove aggregates. The resulting particles were centrifuged and washed three times with deionized water and then stored in phosphate-buffered saline (PBS) pH 7.4 at 4 °C. Particle sizes were determined by dynamic light scattering (DLS, Brookhaven 90Plus Particle Size Analyzer). Gold/lipid mass ratios as a function of Au-NC diameter were measured using DLS (for size), UV−vis (for gold concentration), and infrared spectrometry (Direct Detect, EMD Millipore, for lipid concentration) after collecting four different size fractions of Au-NCs by CL4B gravity columns. Briefly, 200 μL of as-synthesized Au-NCs in PBS were added to CL4B gravity columns and manually collected four different fractions. Au-NC size distribution in each fraction was determined by DLS. Au-NCs were then disrupted with 0.1% Triton-x 100, and the gold mass in each size fraction was determined by UV−vis absorption at 520 nm, while lipid mass was determined by Direct Detect lipid concentration measurement.

Electron Microscopy Imaging of Au-NCs and Cell Thin Sections. *A. TEM Imaging of Au-NCs.* Lipid nanocaspules in PBS or DI water were diluted to 0.04 mg/mL lipids, and 10 μL of solution was placed
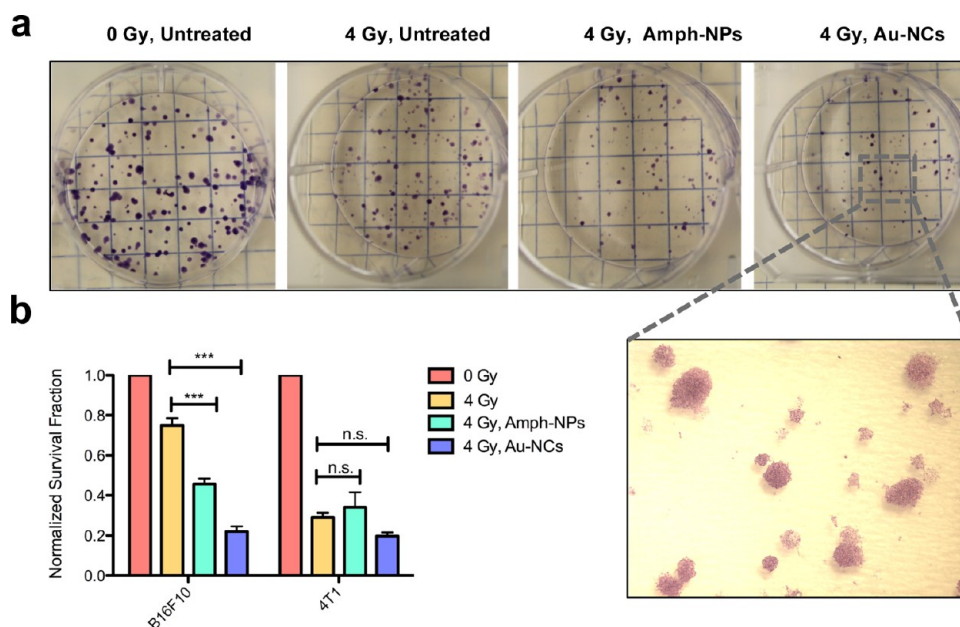
Figure 7. Clonogenic assay assessing radiosensitization promoted by amph-NPs and Au-NCs. B16F10 or 4T1 cells were incubated with amph-NPs (250 nM), Au-NCs (250 nM amph-NPs), or media alone for 24 h at 37 °C and then irradiated with 4 Gy. (a) Growth of B16F10 tumor cell colonies assayed 7 days following 4 Gray of ^{137}Cs γ irradiation, with or without addition of amph-NPs or Au-NCs. (b) Surviving fraction of B16F10 and 4T1 cells (normalized to untreated, unirradiated cells) following irradiation with or without added amph-NPs or Au-NCs. ***, $P < 0.001$ by ANOVA.

on a formvar-coated copper grid, stabilized with evaporated carbon film (Electron Microscopy Sciences, FCF400-Cu). Excess solution was blotted away using filter paper after 20 min. A 1% phosphotungstic acid solution (pH 7) was placed on the grid as a negative stain for 10 s and blotted away using filter paper. The grid was air-dried and stored in a TEM grid storage box until imaged. TEM imaging was conducted using an accelerating voltage of 80 kV on a JEOL 200 CX transmission electron microscope at the Center of Materials Science (CMSE) at MIT.

B. Cryo-EM Imaging of Au-NCs. Au-NC in DI water (3.5 μL) was dropped on a lacy copper grid coated with a continuous carbon film and blotted to remove excess sample without damaging the carbon layer by Gatan Cryo Plunge III. Grid was mounted on a Gatan 626 cryo-holder equipped in the TEM column. The specimen and holder tip were cooled in liquid nitrogen and transferred to imaging stage. Images were recorded on a Gatan 2k × 2k UltraScan CCD camera by a JEOL 2100 FEG microscope operated at 200 kV.

C. TEM Imaging of Tumor Cell Thin Sections. Following amph-NP or Au-NC treatments as indicated in the text, 4T1 or B16F10 tumor cells were washed 2× with pH 7.4 PBS to remove unbound nanoparticles. The cells were fixed in 2.5% gluteraldehyde + 3% paraformaldehyde with 5% sucrose in 0.1 M sodium cacodylate buffer (pH 7.4) for 1 h at 4 °C, pelleted, and post-fixed in 1% OsO_4 in veronal—acetate buffer. The cell pellet was stained in block overnight with 0.5% uranyl acetate in veronal—acetate buffer (pH 6.0), then dehydrated and embedded in Embed-812 resin (Electron Microscopy Sciences). Sections were cut on a Reichert Ultracut E microtome with a Diatome diamond knife at a thickness setting of 50 nm. TEM imaging was conducted with an accelerating voltage of 80 kV using a JEOL 200 CX transmission electron microscope at the Center of Materials Science (CMSE) at MIT.

Confocal Imaging and Colocalization Determination. Cells were seeded in an eight-well chamber (Fisher Scientific Lab-Tek II Chambered Coverglass) at 60000 cells per well in 500 μL of cell culture medium. The cells were allowed to grow overnight to about 80% confluence and then treated with prepared solutions (typical dosage: 250 nM amph-NPs) for 3 or 24 h. Cells were washed twice with PBS and subsequently imaged in RPMI (phenol red free) medium. Confocal laser scanning microscopy was performed on a Zeiss LSM 510 using a 63X oil lens, with excitation wavelengths being 488, 543, and 633 nm.

Colocalization indices and scatter plots of red (OVA) and green (gold) channels were determined by ImageJ software using the FIJI plugin. Representative confocal images ($N = 3$ per cell type) were imported to FIJI, and regions of interest containing three to four cells were defined prior to Pearson's correlation coefficients (PCC) determination. The statistical significance of PCC obtained was determined by the Costes test.

Radiotherapy Studies. Cells were treated with amph-NPs (250 nM) or Au-NCs (250 nM amph-NPs) for 24 h, followed by irradiation with 4 Gy using a ^{137}Cs source. Following irradiation, cells were seeded by limiting dilution at 400 cells per well into six-well culture plates. After 1 week of culture, cell medium was removed, and cells were rinsed with PBS twice and then fixed with 2 mL of a mixture of 6.0% glutaraldehyde and 0.5% crystal violet added to each well at 4 °C for 30 min. The glutaraldehyde crystal violet mixture was carefully immersed in tap water until all excess dye was removed, and plates were air-dried at room temperature. The resulting stained cell colonies were counted using a stereomicroscope.

Conflict of Interest: The authors declare no competing financial interest.

REFERENCES AND NOTES

1. Fisher, B.; Dignam, J.; Wolmark, N.; Mamounas, E.; Costantino, J.; Poller, W.; Fisher, E. R.; Wickerham, D. L.;

Deutsch, M.; Margolese, R.; *et al.* Lumpectomy and Radiation Therapy for the Treatment of Intraductal Breast Cancer: Findings from National Surgical Adjuvant Breast and Bowel Project B-17. *J. Clin. Oncol.* **1998**, *16*, 441–452.

2. Portelance, L.; Chao, K. S. C.; Grigsby, P. W.; Bennet, H.; Low, D. Intensity-Modulated Radiation Therapy (IMRT) Reduces Small Bowel, Rectum, and Bladder Doses in Patients with Cervical Cancer Receiving Pelvic and Para-Aortic Irradiation. *Int. J. Radiat. Oncol. Biol. Phys.* **2001**, *51*, 261–266.

3. Sause, W. T.; Cooper, J. S.; Rush, S.; Ago, C. T.; Cosmatos, D.; Coughlin, C. T.; Janjan, N.; Lipsett, J. Fraction Size in External Beam Radiation Therapy in the Treatment of Melanoma. *Int. J. Radiat. Oncol. Biol. Phys.* **1991**, *20*, 429–432.

4. Jeppesen, S. S.; Schytte, T.; Jensen, H. R.; Brink, C.; Hansen, O. Stereotactic Body Radiation Therapy versus Conventional Radiation Therapy in Patients with Early Stage Non-Small Cell Lung Cancer: An Updated Retrospective Study on Local Failure and Survival Rates. *Acta Oncol.* **2013**, *52*, 1552–1558.

5. Fine, H. A.; Dear, K. B. G.; Loeffler, J. S.; Black, P. M.; Canellos, G. P. Metaanalysis of Radiation Therapy with and without Adjuvant Chemotherapy for Malignant Gliomas in Adults. *Cancer.* **1993**, *71*, 2585–2597.

6. Misawa, M.; Takahashi, J. Generation of reactive oxygen species induced by gold nanoparticles under x-ray and UV Irradiations. *Nanomedicine* **2011**, *7*, 604–614.

7. Rong, Y.; Welsh, J. S. Dosimetric and Clinical Review of Helical Tomotherapy. *Expert Rev. Anticancer Ther.* **2011**, *11*, 309–320.

8. Xing, L.; Thorndyke, B.; Schreibmann, E.; Yang, Y.; Li, T. F.; Kim, G. Y.; Luxton, G.; Koong, A. Overview of Image-Guided Radiation Therapy. *Med. Dosim.* **2006**, *31*, 91–112.

9. Santos Mello, R.; Callisen, H.; Winter, J.; Kagan, A. R.; Norman, A. Radiation Dose Enhancement in Tumors with Iodine. *Med. phys* **1983**, *10*, 75–78.

10. Jordan, A.; Scholz, R.; Wust, P.; Fahling, H.; Felix, R. Magnetic Fluid Hyperthermia (MFH): Cancer Treatment with AC Magnetic Field Induced Excitation of Biocompatible Superparamagnetic Nanoparticles. *J. Magn. Magn. Mater.* **1999**, *201*, 413–419.

11. O'Neal, D. P.; Hirsch, L. R.; Halas, N. J.; Payne, J. D.; West, J. L. Photo-Thermal Tumor Ablation in Mice Using Near Infrared-Absorbing Nanoparticles. *Cancer Lett.* **2004**, *209*, 171–176.

12. Hainfeld, J. F.; Slatkin, D. N.; Smilowitz, H. M. The Use of Gold Nanoparticles to Enhance Radiotherapy in Mice. *Phys. Med. Biol.* **2004**, *49*, N309–N315.

13. Lin, M.-H.; Hsu, T.-S.; Yang, P.-M.; Tsai, M.-Y.; Perng, T.-P.; Lin, L.-Y. Comparison of Organic and Inorganic Germanium Compounds in Cellular Radiosensitivity and Preparation of Germanium Nanoparticles As a Radiosensitizer. *Int. J. Radiat. Biol.* **2009**, *85*, 214–226.

14. Klein, S.; Sommer, A.; Distel, L. V. R.; Neuhuber, W.; Kryschi, C. Superparamagnetic Iron Oxide Nanoparticles As Radiosensitizer *via* Enhanced Reactive Oxygen Species Formation. *Biochem. Biophys. Res. Commun.* **2012**, *425*, 393–397.

15. Douple, E. B.; Richmond, R. C. Platinum Complexes As Radiosensitizers of Hypoxic Mammalian Cells. *Br. J. Cancer Suppl.* **1978**, *3*, 98–102.

16. Chithrani, D. B.; Jelveh, S.; Jalali, F.; van Prooijen, M.; Allen, C.; Bristow, R. G.; Hill, R. P.; Jaffray, D. A. Gold Nanoparticles As Radiation Sensitizers in Cancer Therapy. *Radiat. Res.* **2010**, *173*, 719–728.

17. Zhang, X.-D.; Chen, J.; Luo, Z.; Wu, D.; Shen, X.; Song, S.-S.; Sun, Y.-M.; Liu, P.-X.; Zhao, J.; Hui, S.; *et al.* J. Enhanced Tumor Accumulation of Sub-2 nm Gold Nanoclusters for Cancer Radiation Therapy. *Adv. Healthc. Mater.* **2014**, *3*, 133–141.

18. Hainfeld, J. F.; Dilmanian, F. A.; Slatkin, D. N.; Smilowitz, H. M. Radiotherapy Enhancement with Gold Nanoparticles. *J. Pharm. Pharmacol.* **2008**, *60*, 977–985.

19. Hainfeld, J. F.; Dilmanian, F. A.; Zhong, Z.; Slatkin, D. N.; Kalef-Ezra, J. A.; Smilowitz, H. M. Gold Nanoparticles Enhance the Radiation Therapy of a Murine Squamous Cell Carcinoma. *Phys. Med. Biol.* **2010**, *55*, 3045–3059.

20. Jain, S.; Hirst, D. G.; O'Sullivan, J. M. Gold Nanoparticles As Novel Agents for Cancer Therapy. *Br. J. Radiol.* **2012**, *85*, 101–113.

21. Joh, D. Y.; Sun, L.; Stangl, M.; Al Zaki, A.; Murty, S.; Santoiemma, P. P.; Davis, J. J.; Baumann, B. C.; Alonso-Basanta, M.; Bhang, D.; *et al.* Selective Targeting of Brain Tumors with Gold Nanoparticle-Induced Radiosensitization. *PLoS One* **2013**, *8*.

22. Zaki, A. A.; Joh, D.; Cheng, Z.; Branco De Barros, A. L.; Kao, G.; Dorsey, J.; Tsourkas, A. Gold-Loaded Polymeric Micelles for Computed Tomography-Guided Radiation Therapy Treatment and Radiosensitization. *ACS Nano* **2014**, *8*, 104–112.

23. Zhang, X.-D.; Wu, D.; Shen, X.; Chen, J.; Sun, Y.-M.; Liu, P.-X.; Liang, X.-J. Size-Dependent Radiosensitization of PEG-coated Gold Nanoparticles for Cancer Radiation Therapy. *Biomaterials* **2012**, *33*, 6408–6419.

24. McMahon, S. J.; Hyland, W. B.; Muir, M. F.; Coulter, J. A.; Jain, S.; Butterworth, K. T.; Schettino, G.; Dickson, G. R.; Hounsell, A. R.; O'Sullivan, J. M.; *et al.* Biological Consequences of Nanoscale Energy Deposition Near Irradiated Heavy Atom Nanoparticles. *Sci. Rep.* **2011**, *1*, 18.

25. Singh, C.; Ghorai, P. K.; Horsch, M. A.; Jackson, A. M.; Larson, R. G.; Stellacci, F.; Glotzer, S. C. Entropy-Mediated Patterning of Surfactant-Coated Nanoparticles and Surfaces. *Phys. Rev. Lett.* **2007**, *99*, 4.

26. Verma, A.; Uzun, O.; Hu, Y. H.; Hu, Y.; Han, H. S.; Watson, N.; Chen, S. L.; Irvine, D. J.; Stellacci, F. Surface-Structure-Regulated Cell-Membrane Penetration by Monolayer-Protected Nanoparticles. *Nat. Mater.* **2008**, *7*, 588–595.

27. Jewell, C. M.; Jung, J. M.; Atukorale, P. U.; Carney, R. P.; Stellacci, F.; Irvine, D. J. Oligonucleotide Delivery by Cell-Penetrating "Striped" Nanoparticles. *Angew. Chem. Int. Ed. Engl.* **2011**, *50*, 12312–12315.

28. Sabella, S.; Carney, R. P.; Brunetti, V.; Malvindi, M. A.; Al-Juffali, N.; Vecchio, G.; Janes, S. M.; Bakr, O. M.; Cingolani, R.; Stellacci, F.; *et al.* P. A General Mechanism for Intracellular Toxicity of Metal-Containing Nanoparticles. *Nanoscale* **2014**Published Online.

29. Van Lehn, R. C.; Atukorale, P. U.; Carney, R. P.; Yang, Y.-S.; Stellacci, F.; Irvine, D. J.; Alexander-Katz, A. Effect of Particle Diameter and Surface Composition on the Spontaneous Fusion of Monolayer-Protected Gold Nanoparticles with Lipid Bilayers. *Nano Lett.* **2013**, *13*, 4060–4067.

30. Ernsting, M. J.; Murakami, M.; Roy, A.; Li, S. D. Factors Controlling the Pharmacokinetics, Biodistribution and Intratumoral Penetration of Nanoparticles. *J. Control. Release.* **2013**, *172*, 782–794.

31. Prabhakar, U.; Maeda, H.; Jain, R. K.; Sevick-Muraca, E. M.; Zamboni, W.; Farokhzad, O. C.; Barry, S. T.; Gabizon, A.; Grodzinski, P.; Blakey, D. C. Challenges and Key Considerations of the Enhanced Permeability and Retention Effect for Nanomedicine Drug Delivery in Oncology. *Cancer Res.* **2013**, *73*, 2412–2417.

32. Moon, J. J.; Suh, H.; Bershteyn, A.; Stephan, M. T.; Liu, H. P.; Huang, B.; Sohail, M.; Luo, S.; Um, S. H.; Khant, H.; *et al.* Interbilayer-Crosslinked Multilamellar Vesicles As Synthetic Vaccines for Potent Humoral and Cellular Immune Responses. *Nat. Mater.* **2011**, *10*, 243–251.

33. Andersen, O. S.; Koeppe, R. E., II Bilayer Thickness and Membrane Protein Function: An Energetic Perspective. *Annu. Rev. Biophys. Biomol. Struct.* **2007**, *36*, 107–130.

34. Mashaghi, A.; Partovi-Azar, P.; Jadidi, T.; Nafari, N.; Maass, P.; Tabar, M. R. R.; Bonn, M.; Bakker, H. J. Hydration Strongly Affects the Molecular and Electronic Structure of Membrane Phospholipids. *J. Chem. Phys.* **2012**, *136*, 114709.

35. Carney, R. P.; Carney, T. M.; Mueller, M.; Stellacci, F. Dynamic Cellular Uptake of Mixed-Monolayer Protected Nanoparticles. *Biointerphases* **2012**, *7*, 17.

36. Monzavi-Karbassi, B.; Stanley, J. S.; Hennings, L.; Jousheghany, F.; Artaud, C.; Shaaf, S.; Kieber-Emmons, T. Chondroitin sulfate glycosaminoglycans as major P-selectin ligands on metastatic breast cancer cell lines. *Int. J. Cancer.* **2007**, *120*, 1179–1191.

37. Franken, N. A. P.; Rodermond, H. M.; Stap, J.; Haveman, J.; van Bree, C. Clonogenic Assay of Cells *in vitro*. *Nat. Protoc.* **2006**, *1*, 2315–2319.